X-ray diffraction, optical birefringence, and ^{87}Rb nuclear magnetic resonance spectroscopy of the paraelectric and antiferroelectric phases of $Rb_3D_xH_{1-x}(SO_4)_2$

2002 J. Phys.: Condens. Matter 14 895

(http://iopscience.iop.org/0953-8984/14/4/322)

INSTITUTE OF PHYSICS PUBLISHING JOURNAL OF PHYSICS: CONDENSED MATTER

J. Phys.: Condens. Matter **14** (2002) 895–913 PII: S0953-8984(02)28087-X

X-ray diffraction, optical birefringence, and ^{87}Rb nuclear magnetic resonance spectroscopy of the paraelectric and antiferroelectric phases of $Rb_3D_xH_{1-x}(SO_4)_2$

A Titze[1,5], J Kusz[2,3], H Böhm[2], H-J Weber[4] and R Böhmer[1,4]

[1] Institut für Physikalische Chemie, Johannes Gutenberg-Universität, 55099 Mainz, Germany
[2] Institut für Geowissenschaften, Johannes Gutenberg-Universität, 55099 Mainz, Germany
[3] Institute of Physics, University of Silesia, 40-007 Katowice, Poland
[4] Institut für Physik, Universität Dortmund, 44221 Dortmund, Germany

E-mail: Roland.Bohmer@Uni-Dortmund.de

Received 20 August 2001, in final form 9 November 2001
Published 18 January 2002
Online at stacks.iop.org/JPhysCM/14/895

Abstract

The antiferroelectric (AFE) phase transition of $Rb_3D_xH_{1-x}(SO_4)_2$ was studied using x-ray diffraction, optical birefringence, and nuclear magnetic resonance. The orientation dependence of the resonance lines deduced from the quadrupole-perturbed ^{87}Rb nuclear magnetic resonance of $Rb_3D(SO_4)_2$ single crystals indicates slight deviations from the monoclinic symmetry in the paraelectric and the AFE phases. The dynamical critical exponents as deduced from measurements of the spin–lattice relaxation times depend on the deuteron concentration. Additionally, we have carried out x-ray single-crystal diffraction as well as optical birefringence measurements and find clear evidence for a structural phase transition in $Rb_3D(SO_4)_2$. The low-temperature space group of this compound is $A2$.

1. Introduction

The structure and dynamics of hydrogen bonds constitute an active field of research, because H bonds play important roles, e.g., in the properties of bio-polymers, in our understanding of aqueous systems, and in the physics of crystalline and amorphous ice phases [1][6]. Furthermore, in many cases isotope effects are observed. A well known example is furnished by the melting point of D_2O ice which is about 3.8 K higher than that of H_2O ice. At elevated pressures much more pronounced isotope effects have been reported: at 65 GPa, the cubic phase of

[5] Present address: Robert Bosch GmbH, 71701 Schwieberdingen, Germany.
[6] For recent surveys, see [2].

deuterated ice VII transforms to tetragonal ice VIII at 120 K. At the same pressure, protonated ice VII exhibits no phase transition down to the lowest temperatures [3]. In D_2O the transition from phase VII to VIII is accompanied by an antiferroelectric (AFE) ordering of the three-dimensionally hypernetted hydrogen-bond network.

Isotope effects are also known for other crystals which exhibit ferroelectrically or antiferroelectrically ordered low-temperature phases [4][7]. The most prominent group of crystals in this context is the KH_2PO_4 (KDP) family for which the three-dimensional (3D) H-bond network shows only an incomplete isotope effect [5]. This means that the fully protonated samples still exhibit finite ordering temperatures. Similar observations have been made in 2D [6] and 1D [7,8] networks and even for so-called zero-dimensional 'networks'. An example for the latter are crystals from the $M_3H(XO_4)_2$ family with $M = \{K, Rb, NH_4\}$, $H = \{H, D\}$, and $X = \{S, Se\}$. Here the hydrogen bonds connect two sulphate or selenate tetrahedra to the ionic group $[(XO_4)\cdot H\cdots(XO_4)]^{3-}$. Remarkably, for several tri-alkali–hydrogen disulphates or diselenates the isotope effect is complete, i.e., the deuterated samples order electrically while no ordering occurs in the protonated samples. Such a behaviour is exhibited, e.g., for $K_3D_xH_{1-x}(SO_4)_2$, $Rb_3D_xH_{1-x}(SO_4)_2$, and $Rb_3D_xH_{1-x}(SeO_4)_2$, with x designating the deuteron concentration. Also some organic crystals with zero-dimensional 'networks' show no proton ordering at low temperatures [9].

Many efforts in this field are directed towards achieving an understanding of the driving forces which lead to the establishment or the suppression of low-temperature electrically ordered phases. Basically there are two major scenarios that are discussed as possible origins of the isotope effect. The first emphasizes the importance of tunnelling effects in protonated crystals leading to a partial or even full suppression of the electrical order seen in the corresponding deuterated compounds. Thus, the disordered paraelectric phase is stabilized quantum mechanically, justifying calling these materials quantum paraelectrics. The second view is based on the observation that for each family of isostructural hydrogen-bonded crystals there is an approximate linear relation between the $O\cdot H\cdots O$ bond length, $R_{OO}(T_C)$, and the phase transition temperature, T_C [10]. This phenomenon has been called the geometric isotope effect in order to emphasize that quantum-mechanical effects (other than those determining the length of the hydrogen bond itself) are not thought to be the most important ones. For the explanation of the Ubbelohde effect (which addresses the dependence of R_{OO} on the degree of deuteration), numerous models have been proposed [11]. A critical test of the notion of a geometric isotope effect should be possible when varying R_{OO} other than by means of temperature—e.g., by the application of external pressure. In this respect it is interesting to note that pressure-dependent neutron scattering investigations revealed that the phase transition temperature of KDP crystals depends not only on R_{OO} (as adjusted by means of pressure) but also on the degree of deuteration [12].

For a theoretical description of the hydrogen isotope effect, one may distinguish those approaches which start from a direct proton–proton coupling from those which explicitly take the proton–environment interactions into account. Direct proton–proton couplings are involved in the classical 'ice rules' which have been quite successful in describing many aspects of the hydrogen dynamics also, e.g., in the 3D networks [5]. However, the large separation of hydrogen bridges in ionic systems like $M_3H(XO_4)_2$ shows that these rules might not always be applicable.

Frequently the proton–proton interactions are mapped onto the transverse Ising model defined by the Hamiltonian $H = -\sum_{i,j} J_{ij} S_i^z S_j^z - \sum_i \Omega_i S_i^x$ [5, 13]. Here Ω_i denotes the

[7] While here we focus on hydrogen-bonded crystals, it should be noted that $SrTiO_3$ shows an oxygen (^{18}O versus ^{16}O) isotope effect; see [4].

tunnelling frequency, J_{ij} the interaction strengths, and S^z and S^x are longitudinal and transverse components of the pseudo-spins. An early extension of this widely applied approach involved a coupling of the pseudo-spins to optical lattice vibrations. Upon approaching the phase transition the latter were found to soften and to eventually freeze out at T_C [14]. More recent and complete treatments of the coupling between the proton and its environment involved not only the lattice, but also the bilinear coupling to the tunnelling modes, as well as to the polarizability of the tetrahedral ions [15, 16]. This way, there is a potential coupling of displacive degrees of freedom (e.g., the distortions of the tetrahedral ions) to the interacting pseudo-spins for which order/disorder aspects appear more prominent [17]. The more elaborate theories capture several features of the symmetry breaking which takes place in the electrically ordered low-temperature phases.

We should also mention that in the framework of another theoretical approach, based on a coupling between tunnelling and phonon modes, it was suggested that the symmetry of the H bond is broken already in the paraelectric phase [18]. This effect was called 'proton self-trapping' and several subsequent experimental studies were interpreted as confirming the existence of self-trapped proton states [19].

For tests of the applicability of the idea of 'proton self-trapping', systems such as $Rb_3D_xH_{1-x}(SO_4)_2$ appear appealing for several reasons:

(i) This family of crystals exhibits a complete isotope effect. While for $x = 1$ an AFE transition takes place at $T_N = 82$ K, crystals with $x < 0.22$ do not order at low temperatures.
(ii) The absence of direct lattice-mediated proton–proton couplings helps to avoid the difficulties imposed by concepts based on the ice rules.
(iii) The alkali disulphates and diselenates have been well characterized by a number of experimental techniques such as those based on x-ray diffraction [20–26], neutron scattering [27–31], calorimetry [32–34], dielectric properties [35–37], Raman spectra [38, 39], and nuclear magnetic resonance (NMR) [40–47].

Despite the large number of investigations dealing with the $M_3H(XO_4)_2$ family, a number of important issues are still unresolved. Several suggestions have been made regarding the structure of the paraelectric phase. On the basis of x-ray [20, 21] and powder neutron [29, 31] diffraction studies, the monoclinic $A2/a$ structure has been favoured. Recent neutron experiments, on the other hand, revealed the occurrence of reflections which are not allowed for this crystal system [30]. Additionally, on the basis of the NMR observation of three magnetically inequivalent alkali sites, it has been argued that the hydrogen bond is non-centrosymmetric in the paraelectric phase [41]. Later it was pointed out that this finding is fully compatible with an $A2/a$ structure [42]. Furthermore, despite some effort [20, 24, 26], the exact symmetry of the AFE low-temperature phase is not agreed upon.

In this paper, in addition to studying lattice symmetries and order parameters using x-ray diffraction and ^{87}Rb NMR techniques, spin–lattice relaxation experiments were employed to investigate the dynamical critical behaviour of $Rb_3D_xH_{1-x}(SO_4)_2$ crystals with nominal deuteron concentrations $x = 1$, 0.65, and 0.5. Furthermore, optical birefringence measurements were carried out in order to characterize the AFE phase transition in $Rb_3D(SO_4)_2$.

2. Experimental details

Single crystals of $Rb_3D_xH_{1-x}(SO_4)_2$ were synthesized from aqueous solutions as described previously [45]. Small crystals of $Rb_3D(SO_4)_2$ and $Rb_3H(SO_4)_2$ suitable for x-ray analysis

were isolated and checked by taking x-ray Laue photographs. Fragments of good quality single crystals of the approximate dimensions 0.5 mm × 0.5 mm × 0.5 mm were studied using multilayer-monochromatized[8] Cu K_α radiation from a Schneider rotating anode and a four-circle Huber diffractometer with a 250 mm χ-circle. The diffractometer was controlled by a personal computer with the STOE STADI4 program system[9] and equipped with a two-stage closed-cycle helium cooling device (CTI-Cryogenics). The study was performed between 10 K and room temperature. The temperature was controlled to within 0.1 K. The refinement of the cell parameters was carried out by measuring about 60 reflections with high 2ϑ values and their Friedel pairs at both sides of the primary beam. An ω-scan was carried out at $+2\vartheta$ and -2ϑ and ω. The centre of gravity was determined for both scans and the observed 2ϑ was calculated from the difference of the two ω-centres. These results will be free of zero-point errors, absorption effects, and systematic errors resulting from a crystal mis-centring.

The NMR measurements were carried out using the quadrupole-perturbed central transition $(+1/2 \leftrightarrow -1/2)$ of the ^{87}Rb ($I = 3/2$) nucleus. All spectra were recorded at a Larmor frequency of $\nu_L = 85.7$ MHz. The frequency offsets, $\nu - \nu_L$, are given with respect to a solution of RbCl in D_2O. Absorption spectra were obtained with whole-echo acquisition using a 90°–t_{HE}–180° sequence with $t_{HE} = 200$ μs. Due to the relatively long transverse dephasing times of typically 2 ms, this does not lead to a significant loss of magnetization. In order to perform the angle-resolved measurements near 78 K, the temperature was kept stable to within ± 0.05 K for several days [45, 53]. ^{87}Rb spin–lattice relaxation times were measured at 85.7 MHz (for $x = 0.5$ and 1) and 107.0 MHz ($x = 0.65$) using powdered samples.

In order to determine the optical birefringence, $\Delta n = n_b - n_a$, a (001) plate of $Rb_3D(SO_4)_2$ was mounted between two polarizers within the sample compartment of an optical two-beam spectrometer [48]. The angle between the principal axes and the birefringent plate was 45°. In this configuration the transmitted intensity, I, is connected to Δn by $I_\perp \propto I_0 \sin^2(\pi\, \Delta n\, d/\lambda)$ or by $I_\parallel \propto I_0 \cos^2(\pi\, \Delta n\, d/\lambda)$ with d denoting the thickness of the sample. $I_\perp$ and $I_\parallel$ refer to the intensities with crossed and with parallel orientations of the polarizers, respectively. The relative intensity was recorded as a function of the wavelength λ in the range 230 nm $< \lambda <$ 2600 nm. The birefringence Δn was determined at those wavelengths which exhibit maxima or minima of $I_\perp$ and of $I_\parallel$.

3. X-ray diffraction

The temperature dependence of the lattice parameters is shown in figure 1. If the differences between the volumes and the two lattice parameters c are plotted as a function of temperature, a discontinuity is observed between 80 and 85 K (figure 2). This indicates that a phase transition occurs in this temperature range[10].

The x-ray diffraction pattern at room temperature is consistent with the space group $A2/a$ which was also found for the isostructural compounds $Rb_3D(SeO_4)_2$ [30], $Rb_3H(SeO_4)_2$ [49], $K_3D(SO_4)_2$ [21], $K_3H(SO_4)_2$ [22], and $K_3H(SeO_4)_2$ [50], whereas from neutron diffraction Gustafsson *et al* [30] find $A2$ for $Rb_3H(SeO_4)_2$ at room temperature.

Below the phase transition temperature of $Rb_3D(SO_4)_2$, superstructure reflections appear in the diffraction pattern which can be described by two wavevectors $\boldsymbol{q}_1 = (0, 1/2, 1/2)$ and $\boldsymbol{q}_2 = (0, 1/2, -1/2)$. Therefore, the low-temperature structure of $Rb_3D(SO_4)_2$ must be described in a cell $(\boldsymbol{a}, 2\boldsymbol{b}, 2\boldsymbol{c})$. For the indexing based on this cell the temperature variation of the reflection $(-1, 3, 5)$ is shown in figure 3. $Rb_3D(SO_4)_2$ exhibits the appearance of the

[8] A monochromator from OSMIC Incorporated, Troy, MI, USA was employed.

[9] From the 1995 STADI4 Software Manual, Stoe & Cie, Darmstadt, Germany.

[10] It should be noted that, from calorimetry, T_N for $Rb_3D(SO_4)_2$ was reported to be 78.5 K [34], while our crystals order at 82 K probably due to slight differences in the degree of deuteration.

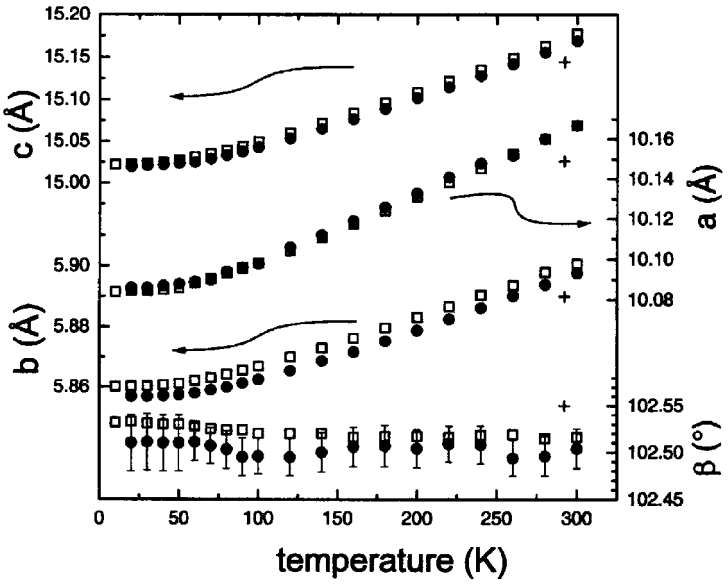

Figure 1. The lattice parameters as a function of temperature for $Rb_3D(SO_4)_2$ (filled circles) and $Rb_3H(SO_4)_2$ (open squares) from this work. The error bars for the lattice constants are smaller than the size of the symbols. The crosses mark data for $Rb_3H(SO_4)_2$ from [27].

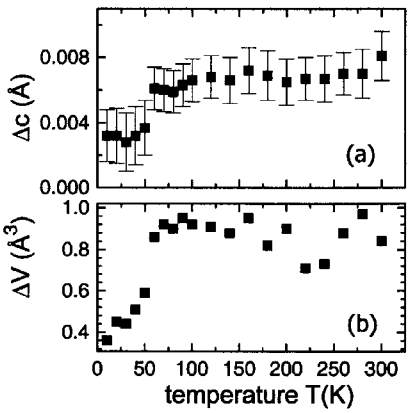

Figure 2. Differences between (a) the lattice parameters c with $\Delta c \equiv c(Rb_3H(SO_4)_2) - c(Rb_3D(SO_4)_2)$ and (b) the cell volumes with $\Delta V = V(Rb_3H(SO_4)_2) - V(Rb_3D(SO_4)_2)$ as a function of temperature. For both quantities, discontinuities are clearly seen near T_N.

superstructure reflection whereas $Rb_3H(SO_4)_2$ does not show any phase transition. Thus, $Rb_3D_xH_{1-x}(SO_4)_2$ exhibits the same behaviour as it is known for $K_3D_xH_{1-x}(SO_4)_2$ [24, 26]. The data on $Rb_3D(SO_4)_2$ have been taken upon cooling and heating. There is no thermal hysteresis which is indicative of a second-order phase transition.

For $K_3D(SO_4)_2$, Noda *et al* [24, 26] find that a cell doubling occurs along the $\boldsymbol{b}$- and $\boldsymbol{c}$-directions and that systematic absences of an A lattice are observed when the indexing is based on a $(\boldsymbol{a}, 2\boldsymbol{b}, 2\boldsymbol{c})$ superstructure. Since there are weak reflections at $h = 2n + 1$ the structure does not involve an a-glide plane. The low-temperature phase for $K_3D(SO_4)_2$ must therefore be taken as $A2$. Other possibilities, $A2/m$ and Am, are ruled out because of the continuity

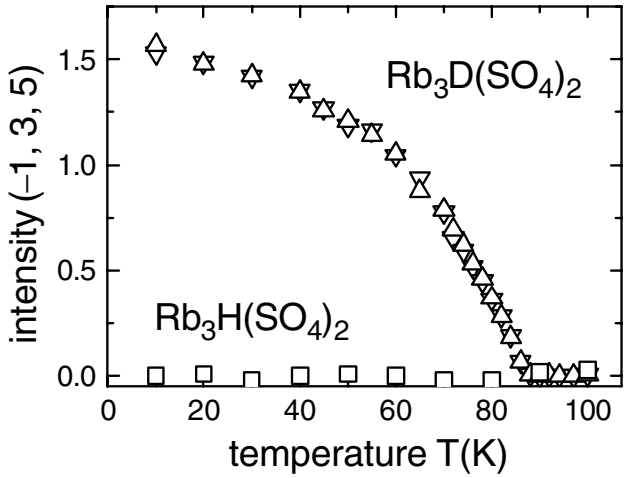

Figure 3. Intensity variation of the reflection $(\bar{1}35)$ from x-ray diffraction as a function of temperature for $Rb_3H(SO_4)_2$ (squares) and for $Rb_3D(SO_4)_2$ (triangles) as measured upon cooling and heating. The error bars are smaller than the size of the symbols.

of the symmetry elements from the $A2/a$ space group at high temperatures. In the $A2$ phase, there are eight non-equivalent SO_4^{2-} molecules and, even though the space group is $A2$, there is a pseudo-symmetry of an a-glide plane and the structure is very close to $A2/a$. Our diffraction pattern shows reflections only for $h + k = 2n$ but there are also reflections for $h = 2n + 1$. The condition for an A lattice is fulfilled but not the one for the a-glide plane. Therefore, we conclude that the space group of $Rb_3D(SO_4)_2$ at low temperatures is $A2$.

4. NMR spectroscopy

4.1. Central-transition spectra of $Rb_3D(SO_4)_2$

Previously, rotation patterns of the deuterium resonance frequencies of $Rb_3D(SO_4)_2$ were reported above and below T_N [44]. For ^{87}Rb, corresponding information is so far only available at room temperature [42]. At 300 K the number of lines and their angular dependence were found to be consistent with the monoclinic space group $A2/a$. Recent neutron diffraction experiments carried out in the paraelectric phase of $Rb_3H(SeO_4)_2$ indicated, however, that upon lowering the temperature, reflections develop which should be extinct in this crystal system [30]. This calls for more extensive NMR studies, since this method is highly sensitive to changes in the local symmetry.

Using ^{87}Rb NMR we have recorded the angular dependence of the resonance frequencies of the central $(+1/2 \leftrightarrow -1/2)$ lines in the paraelectric phase of $Rb_3D(SO_4)_2$ at $T = 100$ K. To this end we have rotated a $Rb_3D(SO_4)_2$ single crystal about three mutually perpendicular axes α denoted as u, v, and w. The resulting rotation patterns, i.e., the line shifts, $(\nu - \nu_L)_\alpha$, versus the rotation angles, θ_α, are shown in figure 4. It is pointed out that the rotation axis u is collinear with the monoclinic c^*-axis (to within $<2^\circ$). In figure 4(a) we have marked the orientations at which the monoclinic a- and b-axes are parallel to the external magnetic field. The starting position corresponding to the rotation axis v is also shown. In figure 4(a) the resonance frequency of one site (the Rb(1) site) is only weakly modulated, indicating that the largest principal axis of the associated electric field gradient (EFG) tensor is almost

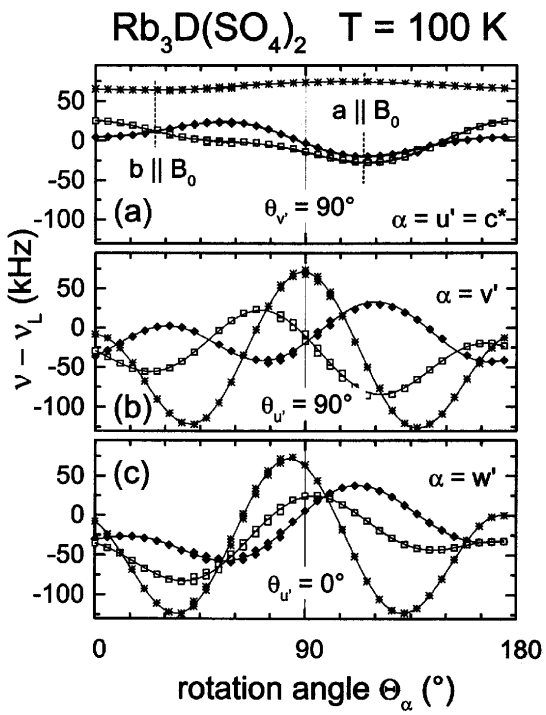

Figure 4. Orientation-dependent positions of the resonance lines of the central ^{87}Rb transition. The data were obtained by rotating the crystal about three mutually perpendicular axes through the angles θ_α. The crosses correspond to the Rb(1) site, the other symbols to the Rb(2) sites. In frame (a) we have marked the angles at which the crystallographic axes *a* and *b* are aligned parallel to the static external magnetic field. Other special orientations are also labelled. The curves are fits using equation (1) and the resulting tensor parameters are given in table 1. The data were obtained at 100 K, i.e., above the AFE phase transition temperature.

parallel to u (or c^*). With respect to the angle for which $\boldsymbol{b} \parallel \boldsymbol{B}_0$, the $\theta_{u'}$-dependences of the other two lines exhibit an approximate mirror symmetry. Thus these resonances refer to the crystallographically equivalent but magnetically inequivalent Rb(2′) and Rb(2″) sites. The assignment of lines for the other rotation axes follows directly from the fact that in specific corresponding orientations the line splittings are identical; cf. figure 4.

More quantitatively, the full orientation dependence for each site was described by a set of 15 coefficients, $d_{i,\alpha}$ (i.e., five for each of the three rotation axes). For each rotation axis α, the expression is [51]

$$(\nu - \nu_L)_\alpha = -\nu_Q^2[d_{0,\alpha} + d_{1,\alpha}\sin(2\theta_\alpha) + d_{2,\alpha}\cos(2\theta_\alpha) + d_{3,\alpha}\sin(4\theta_\alpha) + d_{4,\alpha}\cos(4\theta_\alpha)]/(96\nu_L V_{ZZ}^2). \quad (1)$$

Here $\nu_Q = eQV_{ZZ}/2h$ is the quadrupole coupling constant and $V_{ZZ} = eq$ the largest eigenvalue of the EFG in the principal axis system (PAS) of the tensor. For convenience, below, we will give not only ν_Q but also the tensor components V_{ij} in units of frequency. Fits using equation (1) are shown as solid curves in figure 4. From the five parameters thus obtained for each rotation axis, only $d_{3,\alpha}$ and $d_{4,\alpha}$ are used (since $d_{0,\alpha}$ is independent of the orientation, and $d_{1,\alpha}$ as well as $d_{2,\alpha}$ additionally depend on first-order effects, e.g., the chemical shift anisotropy [52]). From these six coefficients (i.e., two for each rotation axis) one can determine the five EFG parameters for each site, i.e., the three principal values and the polar and the azimuthal angles specifying the tensor orientation in a given reference frame.

Table 1. Tensor components V_{ij} (in MHz) at the ^{87}Rb site of $Rb_3D(SO_4)_2$ in the orthogonal pseudo-monoclinic a, b, c^* system based on the analysis of the 100 K data shown in figure 4. The largest principal value in the PAS, V_{ZZ}, and the asymmetry parameter, η, are also given. All tensor components shown (as well as V_{XX} and V_{YY}) are accurate to within about 30 kHz. Consequently the uncertainty in the asymmetry parameter, $\eta \equiv (V_{XX} - V_{YY})/V_{ZZ}$, is 0.02 or smaller.

	V_{aa}	V_{bb}	$V_{c^*c^*}$	V_{ab}	V_{ac^*}	V_{bc^*}	V_{ZZ}	η
Rb(1)	−2.92	−2.73	5.65	−0.03	−0.03	−0.03	5.65	0.04
Rb(2′)	−1.55	−0.82	2.38	−1.51	1.02	−2.02	3.84	0.38
Rb(2″)	−1.44	−0.94	2.39	1.43	1.40	1.81	3.83	0.46

In table 1 we summarize the six components of the symmetric and traceless EFG tensor in the a, b, c^* coordinate system. Since the off-diagonal elements for the Rb(1) tensor are very small, one recognizes that the principal axes are essentially oriented along the monoclinic axes a, b, and c^*. Furthermore, the asymmetry parameter, $\eta \equiv |V_{aa} - V_{bb}|/V_{c^*c^*}$, is almost zero for the Rb(1) site. In particular, these findings are compatible with Rb(1) being located on a symmetric site and a twofold rotation axis. Both features are expected for $A2/a$. Within this space group the asymmetric Rb(2) units have to obey a (glide) reflection symmetry. This means that all the tensor components in the PAS and consequently V_{ZZ} and η should be the same. While in table 1 it is seen that the V_{ZZ}-values of the Rb(2) sites are identical within experimental error, their asymmetries differ significantly; in particular, the V_{ac^*}-components deviate by about 400 kHz from one another. This finding is incompatible with a monoclinic $A2/a$ system and indicates a lower symmetry which we will call pseudo-monoclinic[11]. This is because the inversion symmetry which results from the combination of (glide) reflection and the perpendicular twofold rotation axis is preserved within experimental error (otherwise more than three lines should appear in the NMR spectra). Furthermore, the deviations from the monoclinic symmetry are so small that they could not be detected from NMR powder spectra [45], and also could not be detected from the x-ray data reported above, and not even from the ^{87}Rb single-crystal rotation patterns of $Rb_3D(SO_4)_2$ recorded at 300 K [45]. This latter finding suggests that the deviations from monoclinic symmetry increase with decreasing temperature already in the paraelectric phase, and this trend is thus compatible with results from neutron diffraction on $Rb_3H(SeO_4)_2$ [30].

On lowering the temperature, the AFE transition in $Rb_3D(SO_4)_2$ takes place at $T_N = 82$ K. This phase transition leads to a quadrupling of the number of NMR frequencies, i.e., twelve resonance lines are generally observed [45]. In order to check the local symmetries we have recorded series of orientation-dependent measurements slightly below T_N. Rotation patterns involving 12 second-order perturbed resonance lines may be anticipated to be quite complex. Therefore, in order to facilitate the assignments of resonance lines and to be able to focus on the deviations from the high-temperature ($T = 100$ K) symmetry, we have used the same specimen as for the measurements at 100 K, reported above. In particular, this implies that the same set of rotation axes u, v, and w was employed for both experiments. In figure 5 we present the angular dependence of the frequency shifts obtained at a temperature of 78.1 K. Overall there are a number of similarities to the rotation patterns recorded at 100 K. At least partly due to the fact that some of the lines exhibit very similar orientational dependences, the proper assignment of the resonances is now considerably more tedious than before. From several independent procedures [53] we were able to determine the set of EFG tensor parameters, and in table 2 we reproduce V_{ZZ} and η for each magnetically inequivalent site. The four lines originating from, e.g., Rb(1) are called Rb$(1, n)$ with $n = 1, 2, 3, 4$. Let us draw attention

[11] This means that the metric is monoclinic and would leave $P\bar{1}$ as a possible space group.

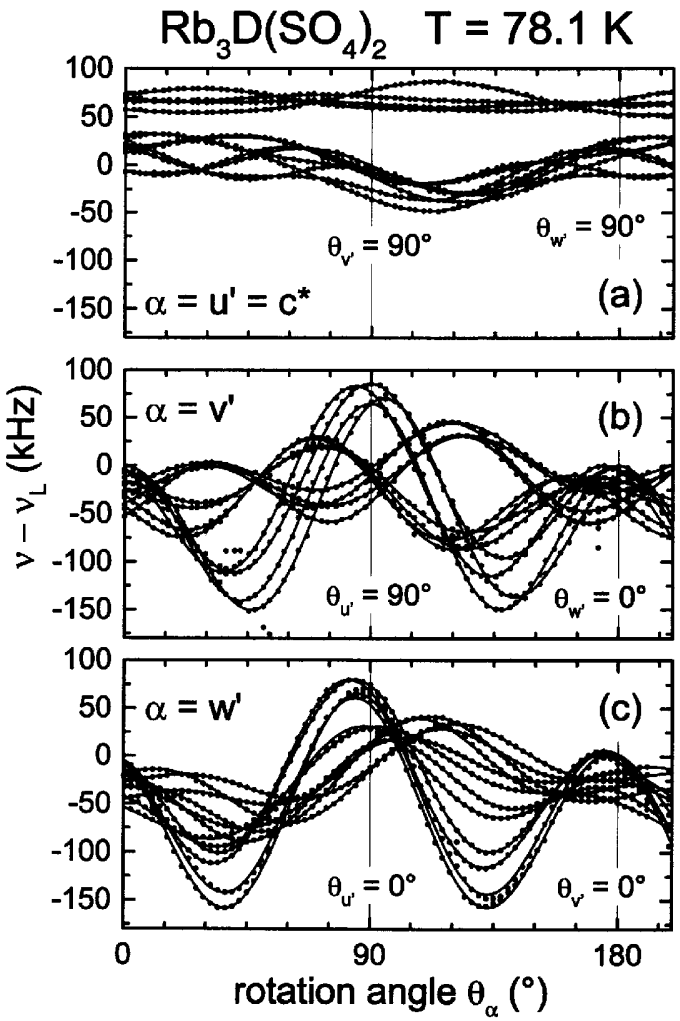

Figure 5. As figure 4, but recorded below the AFE phase transition temperature. The anisotropy and asymmetry parameters corresponding to the solid curves are given in table 2.

to several observations. With the index $s = 2', 2''$ labelling the original asymmetric sites, the averaged principal axis values, $\sum_n \nu_Q[\mathrm{Rb}(s, n)]/4$, within experimental error, are equal to their values, $\nu_Q[\mathrm{Rb}(s)]$, at 100 K. Moreover, as table 2 shows the coefficients for $\mathrm{Rb}(2', n)$ equal those for $\mathrm{Rb}(2'', n)$ for each n within experimental error[12]. Then table 2 shows that the tensor parameters for Rb(1, 1) and Rb(1, 3) are identical to those of Rb(1, 2) and Rb(1, 4), respectively.

However, from inspecting the tensor *orientations* it becomes clear that neither (glide) reflection planes nor twofold axes can unambiguously be defined at low temperatures. A more detailed analysis of the data shown in figure 5 reveals [53] that the tensors of the asymmetric sites ($\mathrm{Rb}(2', n)$ and $\mathrm{Rb}(2'', n)$ for each n) are related approximately (only!) by a twofold rotation

[12] It should be noted, however, that the quadrupole couplings for $\mathrm{Rb}(2', n)$ appear to be systematically larger (albeit slightly) than those for $\mathrm{Rb}(2'', n)$.

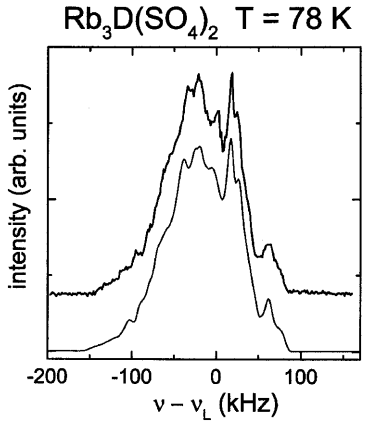

Figure 6. The upper trace reflects the ^{87}Rb central-transition powder spectrum of $Rb_3D(SO_4)_2$. The lower trace is computed using the tensor parameters given in table 2. Excellent agreement is found.

Table 2. Quadrupole couplings in MHz (upper table) and asymmetry parameters (lower table) corresponding to the 12 lines shown in figure 5. It can be seen that there are always two sites for which the coefficients agree within experimental error.

V_{ZZ}	$n = 1$	$n = 2$	$n = 3$	$n = 4$
Rb(1, n)	5.83	5.83	5.70	5.72
Rb(2′, n)	4.20	3.93	3.83	3.56
Rb(2″, n)	4.17	3.91	3.81	3.55
η				
Rb(1, n)	0.21	0.20	0.27	0.27
Rb(2′, n)	0.39	0.35	0.64	0.48
Rb(2″, n)	0.37	0.38	0.65	0.49

around the pseudo-monoclinic b-axis. Furthermore, the Rb(1, 1) and Rb(1, 2) (or Rb(1, 3) and Rb(1, 4)) tensors, corresponding to the symmetric units, exhibit a reflection symmetry with the mirror plane defined by the a–c plane [53]. This implies that twelve crystallographically inequivalent sites should be present, as experimentally observed.

We have also made measurements on a finely powdered sample of $Rb_3D(SO_4)_2$, and in figure 6 we show a spectrum recorded at a temperature of 78 K (upper curve). The lower curve in figure 6 demonstrates that the overall shape can be reproduced by a superposition of six equally weighted powder spectra with the parameters given in table 2. The calculations are described in more detail elsewhere [45, 53]. It is clear that from the powder spectra alone the EFG parameters cannot be extracted. However, the good agreement between the powder pattern and the simulations confirms the results of the (by no means trivial) analysis of the complex rotation pattern recorded for the single crystal.

4.2. Spin–lattice relaxation

The dynamical properties of $Rb_3D_xH_{1-x}(SO_4)_2$ can be studied using spin–lattice relaxation measurements. These essentially allow one to monitor the fluctuations of the EFG at the probe sites on the scale set by the Larmor frequency [54]. Previously, deuteron and rubidium NMR

for fully deuterated samples was used to study the soft mode which drives the AFE phase transition. Since the quadrupolar coupling of the deuterons (<0.1 MHz [44]) is much smaller than that of ^{87}Rb (several MHz [45, 46]), spin–lattice relaxation is very inefficient for the former nucleus. Near the AFE transition of $Rb_3D(SO_4)_2$ a shallow deuteron relaxation time minimum has been reported, but there $^2T_1$ was always longer than 1000 s [44,53]. In the same temperature range and at comparable Larmor frequencies, ^{87}Rb relaxation times, $^{87}T_1$, down to about 30 ms were found [42]. While this renders $^{87}T_1$-measurements relatively fast, the analysis of the data is somewhat complicated by the facts that only selective excitation (of the central transition) is possible [55] and that, in our case, there is a multitude of sites and therefore also of quadrupolar coupling parameters. The resulting multi-exponential longitudinal magnetization recovery may be hard to resolve spectrally below T_N. In this situation it may not even be an advantage to use single crystals. Above T_N, at which the spectra are far less crowded, spectral separation in single crystals is more easily possible and has been accomplished [42]. In the case of deuteron NMR, on the other hand, the spectra seem to be less crowded [44], thus facilitating the study of single crystals also below T_N—however, at the expense of very long measuring times.

In the following we will mainly focus on ^{87}Rb spin–lattice relaxation measurements of powder samples. It should be noted that in the presence of at least three magnetically inequivalent Rb sites, an at least sixfold exponential magnetization recovery is expected in a single crystal. Since the spin–lattice relaxation times are also angle dependent, the determination of the corresponding rates from powder data is impossible. However, the 1/e decay times can be taken as a measure for T_1. In figure 7 we present corresponding data for $Rb_3D(SO_4)_2$, $Rb_3D_{0.65}H_{0.35}(SO_4)_2$, and $Rb_3D_{0.5}H_{0.5}(SO_4)_2$ for a range of temperatures. The phase transition temperatures are signalled by pronounced T_1-minima. These show up at 82, 48, and 21 K for the crystals with deuterium concentrations $x = 1$, 0.65, and 0.5, respectively. In addition to the critical contribution, $T_{1,\mathrm{crit}}$, associated with the AFE transitions, relaxation via lattice vibrations and possibly other effects, $T_{1,\mathrm{latt}}$, also plays a (minor) role. The latter may be estimated from the data for $Rb_3H(SO_4)_2$ which show no phase transition down to the lowest temperatures. The critical contributions, $T_{1,\mathrm{crit}} = 1/(1/T_1 - 1/T_{1,\mathrm{latt}})$, thus obtained are plotted double logarithmically in figures 8(a)–(c). For all concentrations a power-law behaviour, $T_{1,\mathrm{crit}} \propto |T - T_N|^{\lambda}$, is recognized to hold over large temperature ranges below as well as above T_N. The critical exponents, λ, are the same on both sides of T_N, but they depend considerably on the deuteron concentration. For $x = 1$ we find $\lambda = 0.67 \pm 0.07$ (which within experimental error reproduces the results previously obtained in a somewhat smaller temperature range [42]). For $x = 0.5$ and 0.65 the exponents turn out to be $\lambda = 1.15 \pm 0.15$ and 0.87 ± 0.09, respectively. The given error estimates do not reflect the relatively minor scatter in the experimental data, but predominantly the uncertainty in the determination of T_N.

The multi-exponentiality of the longitudinal ^{87}Rb magnetization recovery, $M(t)$, could also be described well using the phenomenological Kohlrausch function, $M(t) \propto \exp[-(t/T_1)^{1-\nu}]$. Here T_1 denotes the 1/e decay time of the magnetization recovery and the exponent ν is a measure for the deviations from exponential spin–lattice relaxation. In figures 8(d)–(f) we present $\nu(T)$ for all concentrations. We find $\nu \approx 0$ in the regime in which T_1 is dominated by lattice vibrations, i.e., if T_N is not closely approached. Indeed a site-resolved measurement far above T_N (not shown) revealed that for each site the magnetization recovery is single exponential ($\nu = 0 \pm 0.03$). Very close to T_N, considerable stretching is observed for all samples. It is remarkable that the deviations from exponentiality are more pronounced for the partially deuterated samples. This finding can tentatively be ascribed to the disorder arising from the random proton/deuteron replacement. In any case, the longitudinal ^{87}Rb relaxation

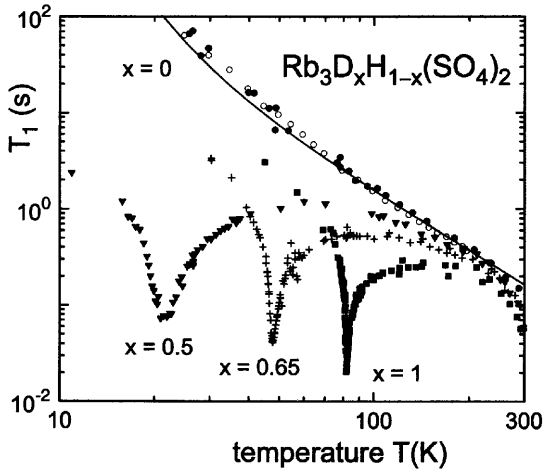

Figure 7. The temperature dependence of the ^{87}Rb spin–lattice relaxation time of $Rb_3D_xH_{1-x}(SO_4)_2$, for several deuteron concentrations x. The concentration-dependent AFE transition temperatures can be inferred from the sharp minima. The sample with $x = 0$ does not exhibit electrical order down to the lowest temperatures. The open circles are taken from [43]. The solid curve represents a model which takes into account the spin–lattice relaxation via lattice vibrations [54].

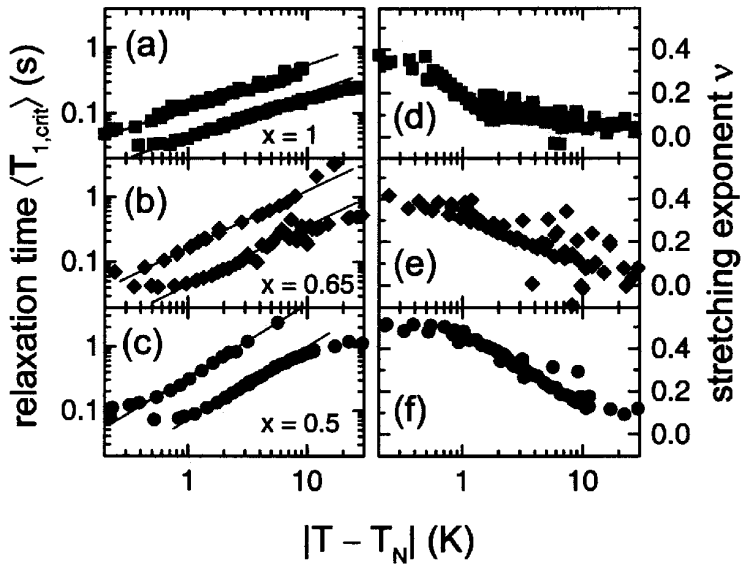

Figure 8. (a)–(c) Double-logarithmic plots of the critical contributions to the ^{87}Rb spin–lattice relaxation times for various deuteron concentrations. The slopes of the curves reflect the corresponding critical exponents λ. (d)–(f) Stretching exponents ν. For $x = 1$ one finds that $\nu > 0$ only close to T_N. It should be noted that the Larmor frequencies are 85.7 MHz for $x = 0.5$ and 1 and 107.0 MHz for $x = 0.65$.

due to EFG fluctuations should at least be double exponential, $M(t) \propto e^{-2W_1 t} + e^{-2W_2 t}$, with the rates [56, 57]

$$W_k = (C^{(\zeta)}\,\Delta V_k)^2 J(k\nu_L) \tag{2}$$

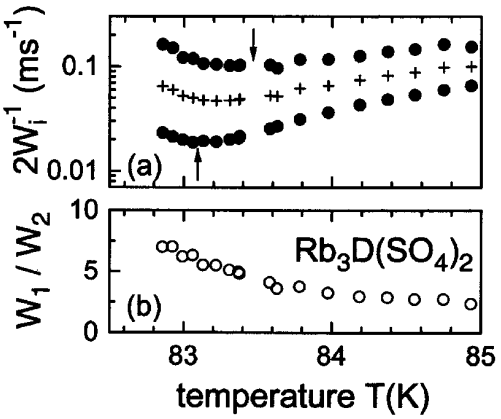

Figure 9. (a) Temperature dependences of the relaxation rates $2/W_1$ and $2/W_2$ from the bimodal ^{87}Rb magnetization recovery of $Rb_3D(SO_4)_2$ at the Rb(2) site near T_N. The average of these rates (corresponding to T_1) is given by the crosses. The arrows highlight that the temperature positions of the minima are slightly different. (b) The ratio of the rates W_1/W_2 increases upon approaching the AFE phase transition temperature from above.

for $k = 1, 2$ and $C^{(\zeta)} = eQ^{(\alpha\zeta)}/[2I(2I-1)\hbar]$. Here $\zeta = 2$ and 87 stand for ^{2}H and ^{87}Rb, respectively. Furthermore, Q is the nuclear quadrupole moment, and $\Delta V_1^2 = 4(\Delta V_{xz}^2 + \Delta V_{yz}^2)$ and $\Delta V_2^2 = \frac{1}{4}(\Delta V_{xx} - \Delta V_{yy})^2 + \Delta V_{xy}^2$ denote different linear combinations of (squares of) fluctuation amplitudes, ΔV_{ij}, of the various EFG tensor elements [56, 57]. Previously we reported for $Rb_3D(SO_4)_2$ that the ratio W_1/W_2 differs significantly from unity in the close vicinity of T_N, only [42]. This is in accord with the temperature dependence of ν; cf. figure 8(d). The above expression for W_k suggests that two limiting scenarios could be invoked to rationalize these observations. If $J(\nu_L)$ equals $J(2\nu_L)$, then these observations are to be related to a relative change of fluctuation amplitudes and hence a change in the orientation dependence of the order parameter fluctuations. Alternatively, a change in the W_1/W_2 ratio may arise solely if the spectral density becomes frequency dependent, $J(\nu_L) \neq J(2\nu_L)$—in other words, if the rate of EFG fluctuations approaches the Larmor frequency. From measurements carried at two different Larmor frequencies on powdered $Rb_3D(SO_4)_2$ it was concluded that $J(\nu_L) \approx J(2\nu_L)$ holds over large ranges of temperature on both sides of T_N [42].

Spectrally resolved T_1-measurements are required in order to check with a better sensitivity whether a frequency dependence of the spectral density can be ruled out also very near T_N or rather has to be taken into account as a possible source of the considerable non-exponentiality. To this end, we have studied the relaxation at the Rb(2) site of a $Rb_3D(SO_4)_2$ single crystal. The results are shown in figure 9. It is clearly seen that the temperature positions in the maxima of W_1 ($\propto J(\nu_L)$) and W_2 ($\propto J(2\nu_L)$) differ by up to about 0.5 K, as evidenced also by similar results for various other orientations [53]. In view of this frequency dependence of the spectral density it becomes clear that near T_N the soft-mode frequency cannot be too far off from ν_L. This would also rationalize the saturation of T_1 seen in figure 8 for $|T - T_N| < 1$ K.

5. Optical birefringence

The inset of figure 10 shows the dispersion of the birefringence Δn of $Rb_3D(SO_4)_2$. Characteristic features are the quadratic dependence of Δn on the photon energy for a wide range of the optical spectrum and its steep decrease at small photon energies. Both features

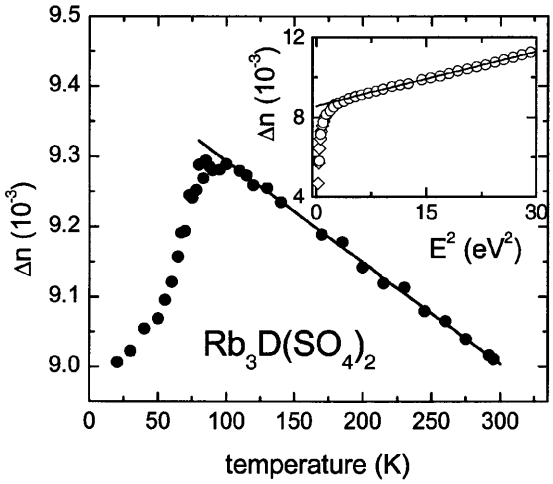

Figure 10. The optical birefringence Δn of $Rb_3D(SO_4)_2$ as measured at a phonon energy $E = 2.8$ eV as a function of temperature. The data have been obtained on cooling and on heating. $\Delta n(T)$ varies linearly above T_N (solid line). In the inset the optical birefringence at room temperature is plotted versus the square of the photon energy E. Circles and diamonds represent data taken for two different samples.

are signatures of the presence of hydrogen bonds [48]. Describing the infrared contribution by a Sellmeier oscillator we find a resonance energy of $E_0 = 0.304$ eV which corresponds to a wavenumber of 2450 cm^{-1}. This is a reasonable value for the vibrational band of D–O bonds. The electronic contribution to Δn, which is illustrated by the solid line in the inset of figure 10, is proportional to $\sum_i (\cos^2 \gamma_b^i - \cos^2 \gamma_a^i)$. Here γ_b (γ_a) denotes the angle enclosed by the D–O bond i and the crystallographic axis b (a). We have evaluated the sum in order to determine the sign of Δn.

In order to elucidate the structural origin of the optical changes with temperature we have carried out measurements for the photon energies 0.48 eV $< E <$ 1.55 eV. In this range, birefringence is produced by a superposition of vibronic and electronic contributions. They have been obtained by exploiting their difference in dispersion apparent in the inset of figure 10. Figure 10 shows the dependence of the electronic contribution to the optical birefringence of $Rb_3D(SO_4)_2$ on temperature. Above T_N we find that Δn increases linearly with decreasing temperatures. The AFE phase transition is clearly marked by the deviations from this simple behaviour and by a decrease in Δn. Furthermore, the birefringence was determined at room temperature also after the sample was rotated by small angles χ ($<15^\circ$) and at low temperatures for two different orientations of the sample. Due to the monoclinic symmetry, large values of $\partial \Delta n / \partial \chi$ have been observed for a rotation about the crystallographic axis b. Comparing the data observed at room temperature and at low temperatures, we realize that the linear increase of birefringence with decreasing temperature (see figure 10) is consistent with a rotation of the optical indicatrix which is characteristic of a simple tilting mode of the O–D–O bonds. To describe the changes below T_N, deformations of the optical indicatrix also have to be taken into account—which indicates a more complex structural origin than above T_N. Over the whole range of temperatures we find no difference in thermal behaviour between the two different contributions to the birefringence.

6. Discussion

Let us first discuss the structural properties of $Rb_3D_xH_{1-x}(SO_4)_2$. Far above T_N, e.g., at room temperature, the results from diffraction [27] as well as from NMR [42] studies are compatible with the monoclinic space group $A2/a$ ($Z = 4$). In particular, from our previous single-crystal NMR studies we concluded that at 300 K the (glide) reflection symmetry expected for $A2/a$ at the Rb(2′) and Rb(2″) sites and the inversion symmetry at the hydrogen sites are obeyed [42, 45]. The rotation patterns of $Rb_3D(SO_4)_2$, recorded in the present work, reveal that at 100 K the inversion symmetry at the centre of the H bond is still preserved. However, the asymmetry parameters for the Rb(2′) and the Rb(2″) sites differ beyond the estimated experimental error (table 1). Let us note that this finding of a slight symmetry departure solely relies on the evaluation of the EFG principal axis values and not on a considerably more uncertain determination of the orientation of the tensors in the crystal axis system. These small deviations from the monoclinic symmetry are not resolved in the present x-ray experiments, in accord with previous studies of related substances [20–22, 24]. From neutron diffraction studies on $Rb_3H(SeO_4)_2$, Bragg reflections indexed as (h 0 l) with odd h and even l, which are ruled out for $A2/a$, were reported to grow when cooling from 300 to 100 K [30]. From the latter study it was concluded that the symmetry departure from $A2/a$ can almost exclusively be ascribed to the H-bond system.

Observations of departures from the symmetry of this space group can also be made in the temperature range $T < T_N$. From our x-ray investigation of $Rb_3D(SO_4)_2$ we have found the space group $A2$, previously reported for the AFE phase of $K_3D(SO_4)_2$ [26], along with a quadrupling of the unit cell. This enlargement of the unit cell is nicely reflected by the quadrupling of the NMR lines; cf. figures 4 and 5. Compatibility with the $A2$ space group implies that the tensors for the Rb(2′, n) sites equal those for the Rb(2″, n) sites, which is only roughly fulfilled.

On the basis of measurements of deuteron spin–lattice relaxation times, it has been argued that the inversion symmetry of the H bond is broken already in the paraelectric phase [46]. Below, we will show that this interpretation is not unambiguous. Before doing so, let us first recall the considerations on which the previously suggested interpretation [46] rests: if the H bond is symmetric, then the EFG tensors which characterize the deuterons in the 'left'-hand and in the 'right'-hand sides of the double-minimum potential can be transformed into one another by an inversion operation. This operation, however, leaves the NMR frequency invariant. Without a modulation of the EFG, the fluctuation amplitude (referred to as ΔV in equation (2)) vanishes and consequently so also does the (intrabond) quadrupolar relaxation rate $1/T_1^{(Q)}$. Experimentally [44, 53], near T_N a very shallow minimum is found for the deuteron T_1. From this observation it was concluded that there is a finite *intra*bond contribution to ΔV and thus a violation of the inversion symmetry of the H bond [44]. In the following we will show that this observation can more naturally be rationalized by taking into account *inter*bond modulations of the EFG at the deuteron site.

To see this more clearly, in figure 11 we have plotted the temperature dependence of the ratio[13] $[\langle {}^2T_1\rangle (C^{(2)})^2]/[\langle {}^{87}T_1\rangle (C^{(87)})^2]$ based on the data for $Rb_3D(SO_4)_2$ given in figure 7 as well as in [44] and [53]. Since the Larmor frequencies employed for the two nuclear probes were compatible, via equation (2) written as $\langle {}^{\zeta}T_1\rangle^{-1} = (C^{(\zeta)}\,\Delta V^{(\zeta)})^2 J(\nu_L)$, the data shown in figure 11 thus correspond to the ratio of the squared fluctuation amplitudes, $(\Delta V^{(87)}/\Delta V^{(2)})^2$. Close to T_N this ratio is about 180 (cf. figure 11). As the following considerations show, this order of magnitude appears very plausible.

[13] The ratio of the squared quadrupole moments of ^{87}Rb and ^{2}H is given by $[Q^{(87)}/Q^{(2)}]^2 = (13/0.28)^2 \approx 2010$; see e.g., the EPR/ENDOR frequency table in the Bruker Almanac of 2000. Thus $[C^{(2)}/C^{(87)}]^2 = 9/2010$.

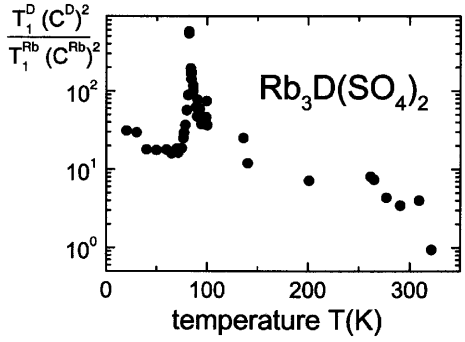

Figure 11. The ratio of squared fluctuation amplitudes as given by $[\langle {}^2T_1\rangle (C^{(2)})^2]/[\langle {}^{87}T_1\rangle (C^{(87)})^2]$. Close to T_N this ratio is near the simple theoretical estimate given in the text.

If a symmetric H bond is assumed to exist just above T_N, then the fluctuation amplitude, $\Delta V^{(2)}$, at the ^{2}H site may be estimated from the simplified expression for the EFG written as $V^{(2)} = \sum_i q_i (r_{i-\mathrm{D}})^{-3}$. Here the sum runs over all adjacent nuclei. This expression for $V^{(2)}$ implies that we drop any angular dependence of the EFG, but retain its distance dependence, within a point charge approach. For small deuteron displacements, $\Delta r_{\mathrm{D-D}}$, the fluctuation amplitude at the probe site is $\Delta V^{(2)} = \sum_i q_i[(r_{i-\mathrm{D}} + \Delta r_{\mathrm{D-D}})^{-3} - (r_{i-\mathrm{D}})^{-3}] = \sum_i q_i[(r_{i-\mathrm{D}})^{-3} - 3\,\Delta r_{\mathrm{D-D}}(r_{i-\mathrm{D}})^{-4} + \cdots - (r_{i-\mathrm{D}})^{-3}] \approx -3\sum_i q_i[\Delta r_{\mathrm{D-D}}(r_{i-\mathrm{D}})^{-4}]$. This expression reduces to $\Delta V^{(2)} \approx -3q_{\mathrm{D}}\,\Delta r_{\mathrm{D-D}}(r_{\mathrm{D-D}})^{-4}$ if the position of only one adjacent deuteron is assumed to be modulated. Similarly, for ^{87}Rb, from $V^{(87)} = \sum_i q_i (r_{i-\mathrm{Rb}})^{-3}$ one obtains that

$$\Delta V^{(87)} \approx -3q_{\mathrm{D}}\,\Delta r_{\mathrm{Rb-D}}(r_{\mathrm{D-Rb}})^{-4} \tag{3}$$

again if solely the distance fluctuation of the nearest deuteron, $\Delta r_{\mathrm{Rb-D}}$, needs to be taken into account. Since any angular dependences have been dropped, the absolute variations of the internuclear vectors are considered the same for all nuclei; in particular, $\Delta r_{\mathrm{D-D}} = \Delta r_{\mathrm{D-Rb}}$. Taken together, these yield the estimate $(\Delta V^{(87)}/\Delta V^{(2)})^2 = (r_{\mathrm{D-D}}/r_{\mathrm{D-Rb}})^8 = (5.1\ \text{Å}/3\ \text{Å})^8 \approx 70$ for the *inter*bond contribution to T_1. In view of the simplifying assumptions made above, the agreement of this ratio with the experimental one is very good. These considerations demonstrate that *intra*bond contributions to the modulation of the EFG at the deuteron sites need not be invoked in order to explain the experimental findings. In other words, in order to understand the shallow minimum in the deuteron spin–lattice relaxation time it is not necessary to assume that the inversion symmetry of the hydrogen bond is broken just above T_N.

The argument just given furthermore shows that near T_N it suffices to take into account only the fluctuations of the hydrogen ions. This suggests that fluctuations of the other nuclei may be relatively small on the scale of the Larmor frequency. Using equation (2) evaluated in the fast-motion regime for the experimental maximum rate, $W \sim 50\ \mathrm{s}^{-1}$ (cf. figure 7), near T_N one obtains the timescale, τ_{C}, on which these fluctuations take place as $\tau_{\mathrm{C}} \sim 10^{-10}$ s. This rough estimate is based on a fluctuation amplitude of $\Delta V \approx 1$ MHz which results from comparing the variations of the EFGs when going from above and to below T_N. The timescale τ_{C} just given is close enough to the Larmor frequency to rationalize the frequency dependence of T_1 in the (very) close vicinity of the AFE phase transition (cf. figure 9). It should be noted from Raman line-shape analyses of $K_3D_xH_{1-x}(SO_4)_2$ at $T_N + 5$ K that a timescale in the range $\tau_{\mathrm{C}} \approx 1\text{–}7 \times 10^{-13}$ s was deduced [38].

A remarkable result from our T_1-measurements is that the dynamic critical exponent λ of $Rb_3D_xH_{1-x}(SO_4)_2$ exhibits a significant deuteron concentration dependence. The exponent

$\lambda = 0.67 \pm 0.07$ for $x = 1$ is similar in magnitude to that of the 3D Ising model[14], the 3D XY model[15], or a generalization thereof[16]. If the soft mode, which drives the phase transition, strongly couples to the dynamics of the hydrogen bonds, then the Ising model appears most appropriate. It is unclear, however, in which way the strong deuteron dependence of λ can be rationalized within this approach since neither the dimensionality nor the type of interaction depends on x in an obvious fashion.

Within an extended transverse Ising model, an anharmonic coupling of the pseudo-spins to the distortion of the adjacent tetrahedral molecular ions (here: SO_4^{2-}) was taken into account [15]. This coupling, which rescales the soft-mode frequency, is a function of the bond length R_{OO} [16] and thus indirectly depends on the deuteron concentration. This model consequently implies that the displacive versus order/disorder character of the transition and thus also the temperature dependence of the soft-mode frequency should show an isotope effect. Therefore, this theoretical approach appears to be in qualitative agreement with the experimental results shown in figure 8. For a more quantitative test the distortion of the sulphate ions would have to be measured. A similar question was recently addressed by ^{31}P chemical shift measurements which allowed detection of the distortions of PO_4 tetrahedra in KH_2PO_4-type ferroelectrics [61]. Due to the somewhat unfavourable NMR properties of sulphur, the prospects of resolving the issue for $Rb_3D_xH_{1-x}(SO_4)_2$ are not really encouraging. However, the investigation of related compounds such as $Rb_3D_xH_{1-x}(SeO_4)_2$ certainly appears worthwhile.

7. Conclusions

We combined ^{87}Rb NMR, optical birefringence, and x-ray diffraction in order to study single-crystalline and powdered tri-rubidium–hydrogen disulphate. An important result of this study is that the inversion centre of the hydrogen bond is conserved in the paraelectric phase. We also pointed out that it is not necessary to invoke asymmetric H bonds in order to rationalize the slight minimum seen in the deuteron spin–lattice relaxation times which was previously interpreted in favour of proton self-trapping.

For the paraelectric as well as in the AFE phases of $Rb_3D_xH_{1-x}(SO_4)_2$, the NMR rotation patterns yield evidence for deviations from the monoclinic symmetry which are, however, not borne out by the x-ray data. This suggests that these symmetry departures are associated with an ordering in the hydrogen-bond system. Below T_N a quadrupling of the unit cell is observed by means of NMR as well as x-ray diffraction. From our x-ray investigations we conclude that for $T < T_N$ the space group of $Rb_3D(SO_4)_2$ is $A2$.

For the critical exponent λ which describes the temperature dependences of the soft-mode frequency, we find a systematic increase for decreasing deuteron concentration. This observation can be rationalized if the displacive versus order/disorder character of the AFE phase transition shows an isotope effect.

Acknowledgments

This research was supported by the Deutsche Forschungsgemeinschaft within project Bo1301/2 and by the 'Materialwissenschaftliches Forschungszentrum der Johannes Gutenberg-

[14] If the characteristic frequency scales with the wavevector of the soft mode like q^z and if the rates W_k couple linearly to the order parameter fluctuations, then $\lambda' = \gamma - \nu(d - z) = 0.61$, where the critical exponents have their usual meaning—see e.g. [58].

[15] Near the incommensurate phase transition of $RbZnCl_2$ one finds $\lambda\ (=2\gamma - 3\nu) = 0.63$ [59].

[16] Here the exponent derived from $\lambda''' = \nu(z - 1 - \eta) = 0.65$ is defined for $T > T_C$ from $1/T_1 \propto [(T - T_C)/T]^{\lambda'''}$; see [60].

Universität, Mainz' (Materials Sciences Centre, Mainz). We thank A Maiazza for growing the crystals used for this work and D Fröhlich for a stimulating discussion.

References

[1] Marx D 1998 *Classical and Quantum Dynamics in Condensed Phase Simulations* ed B J Berne, G Ciccotti and D F Coker (Singapore: World Scientific)
[2] Structural science and various functions in the hydrogen bond 1998 *J. Crystallogr. Soc. Japan* **40** (Special Issue)
Metastable water 2000 *Phys. Chem. Chem. Phys.* **2** (Special Issue)
[3] Pruzan P, Chervin J C and Canny B 1993 *J. Chem. Phys.* **99** 9842
[4] Itoh M, Wang R, Inaguma Y, Yamaguchi T, Shan Y J and Nakamura T 1999 *Phys. Rev. Lett.* **82** 3540
For corresponding predictions for $KTaO_3$, see
Bussmann-Holder A, Büttner H and Bishop A R 2000 *J. Phys.: Condens. Matter* **12** L115
[5] Blinc R and Zeks B 1987 *Ferroelectrics* **72** 193
[6] Dalal N, Klymachyov A and Bussmann-Holder A 1998 *Phys. Rev. Lett.* **81** 5924 and references therein
[7] Albers J 1988 *Ferroelectrics* **78** 3
[8] McMahon M I, Nelmes R J, Kuhs W F, Dorwarth R, Piltz R O and Tun Z 1990 *Nature* **348** 317
Ermark F and Haeberlen U 1991 *J. Phys.: Condens. Matter* **3** 1909
[9] Mochida T, Izuoka A, Sugawara T, Moritomo Y and Tokura Y 1994 *J. Chem. Phys.* **101** 7971
Moritomo Y, Tokura Y, Mochida T, Izuoka A and Sugawara T 1995 *J. Phys. Soc. Japan* **64** 1892
[10] Ichikawa M 1981 *Chem. Phys. Lett.* **79** 583
[11] Sugimoto H 1998 *J. Phys.: Condens. Matter* **10** 1237
Totsuji C and Matsubara T 1998 *Solid State Commun.* **105** 731
[12] Nelmes R J 1988 *J. Phys.: Condens. Matter* **21** L881
[13] Blinc R and Zeks B 1974 *Soft Modes in Ferroelectrics and Antiferroelectrics* (Amsterdam: North-Holland)
[14] Kobayashi K K 1968 *J. Phys. Soc. Japan* **24** 497
[15] Bussmann-Holder A and Michel K H 1998 *Phys. Rev. Lett.* **80** 2173
Bussmann-Holder A, Dalal N and Michel K H 2000 *J. Phys. Chem. Solids* **61** 271
[16] Bussmann-Holder A 1999 *Physica* B **263–4** 643
[17] Katrusiak A 1995 *Phys. Rev.* B **51** 589
[18] Yamada Y 1994 *J. Phys. Soc. Japan* **63** 3756
Ikeda S, Sugimoto H and Yamada Y 1998 *Phys. Rev. Lett.* **81** 5449
[19] Yamada Y and Ikeda S 1994 *J. Phys. Soc. Japan* **63** 3691
[20] Ichikawa M, Gustafsson T and Olovsson I 1992 *Acta Crystallogr.* C **48** 603
[21] Noda Y, Uchiyama S, Kafuku K, Kasatani H and Terauchi H 1990 *J. Phys. Soc. Japan* **59** 2804
[22] Noda Y, Kasatani H, Watanabe Y, Terauchi H and Gesi K 1990 *J. Phys. Soc. Japan* **59** 3249
[23] Noda Y and Kasatani H 1991 *J. Phys. Soc. Japan* **60** 13
[24] Noda Y, Watanabe Y, Kasatani H, Terauchi H and Gesi K 1991 *J. Phys. Soc. Japan* **60** 1972
[25] Noda Y, Kasatani H, Watanabe Y and Terauchi H 1992 *J. Phys. Soc. Japan* **61** 905
[26] Noda Y, Tamura I, Nakao H, Matsuo R and Kuroiwa Y 1994 *J. Phys. Soc. Japan* **63** 1803
[27] Fortier S, Fraser M E and Heyding R D 1985 *Acta Crystallogr.* C **41** 1139
[28] Bohn A, Melzer R, Sonntag R, Lechner R E, Schuck G and Langer K 1995 *Solid State Ion.* **77** 111
[29] Melzer R, Sonntag R and Knight K S 1996 *Acta Crystallogr.* C **52** 1061
[30] Gustafsson T, Ichikawa M and Olovsson I 1998 *J. Korean Phys. Soc.* **32** 199
Gustafsson T, Ichikawa M and Olovsson I 2000 *Solid State Commun.* **115** 473
[31] Onoda-Yamamuro N, Yamamuro O, Matsuo T, Ichikawa M, Ibberson R M and David W I F 2000 *J. Phys.: Condens. Matter* **40** 8559
[32] Fukai M, Inaba A, Matsuo T, Suga H and Ichikawa M 1993 *Solid State Commun.* **87** 939
[33] Fukai M, Matsuo T, Suga H and Ichikawa M 1992 *Solid State Commun.* **84** 545
[34] Matsuo T, Inaba A, Yamamuro O and Onoda-Yamamuro N 2000 *J. Phys.: Condens. Matter* **12** 8595
[35] Gesi K 1980 *J. Phys. Soc. Japan* **48** 886
Gesi K 1992 *J. Phys. Soc. Japan* **61** 162
[36] Endo M, Kaneko T, Osaka T and Maskita Y 1983 *J. Phys. Soc. Japan* **52** 3829
[37] Moritomo Y, Tokura Y, Nagaosa N, Suzuki T and Kumagai K 1993 *Phys. Rev. Lett.* **71** 2833
Moritomo Y, Tokura Y, Nagaosa N, Suzuki T and Kumagai K 1995 *J. Low Temp. Phys.* **99** 55
[38] Kaung P, Kasahara M and Yagi T 1996 *J. Phys. Soc. Japan* **65** 1114 and references therein
[39] Watanabe J, Kasahara M and Yagi T 1999 *Physica* B **263–4** 640

[40] Abramic D, Dolinšek J, Blinc R and Shuvalov L A 1989 *Phys. Rev.* B **42** 442
[41] Takeda S, Kondoh F, Nakamura N and Yamaguchi K 1996 *Physica* B **226** 157
[42] Titze A, Hinze G and Böhmer R 1998 *Phys. Rev.* B **57** R666
[43] Dolinšek J, Mikac U, Javoršek J E, Lahajnar G, Blinc R and Kirpichnikova L F 1998 *Phys. Rev.* B **58** 8445
[44] Mikac U, Arcon D, Zalar B, Dolinšek J and Blinc R 1999 *Phys. Rev.* B **59** 11 293
[45] Titze A, Maiazza A, Hinze G and Böhmer R 1999 *Phys. Rev.* B **59** 11 720
[46] Mikac U, Zalar B, Dolinšek J, Selinger J, Zagar V, Plyushch O and Blinc R 2000 *Phys. Rev.* B **61** 197
[47] Qi F, Winterlich M, Titze A and Böhmer R 2001 unpublished
[48] Weber H-J, Schulz M, Schmitz S, Granzin J and Siegert H 1989 *J. Phys.: Condens. Matter* **1** 8543
[49] Makarova I P, Verin I A and Shchagina N M 1986 *Kristallografiya* **31** 178
[50] Ichikawa M, Gustafsson T and Olovsson I 1994 *Acta Crystallogr.* C **50** 330
[51] e.g., Liechti O and Kind R 1989 *J. Magn. Reson.* **85** 480
[52] Blinc R, Selinger J, Apih T, Dolinšek J, Fuith A, Schranz W and Warhanek H 1995 *Phys. Rev.* B **52** 833
[53] Titze A 2000 *Dissertation* Universität Mainz
[54] Abragam A 1961 *The Principles of Nuclear Magnetism* (Oxford: Oxford University Press)
[55] Han D Y and Kessemeier H 1991 *Phys. Rev. Lett.* **67** 346
[56] Das T P and Hahn E L 1958 *Nuclear Quadrupole Resonance Spectroscopy* (New York: Academic)
[57] e.g., Zumer S and Blinc R 1981 *J. Phys. C: Solid State Phys.* **14** 465
[58] Bjorkstam J L 1974 *Adv. Magn. Reson.* **7** 1
[59] Decker F and Petersson J 2000 *Phys. Rev.* B **61** 8993
[60] Kaufmann B A, Schwabl F and Täuber U C 1998 *Phys. Rev.* B **59** 11 226
[61] Bussmann-Holder A, Dalal N, Fu R and Migoni R 2001 *J. Phys.: Condens. Matter* **13** L231